Parametric Reconstruction of Curved Fibers from Glass fiber-reinforced Composites

Tim Elberfeld[a], Jan Sijbers[a] and Jan De Beenhouwer[a]

[a]*imec-Vision Lab Dept. Physics University of Antwerp Belgium*

ARTICLE INFO

ABSTRACT

In this work, a new framework, called curved Parametric Reconstruction, is proposed, which reconstructs a parametric model of curved fibers from computed tomography scans of glass fiber-reinforced polymers (GFRP). The fiber detection and tracing strategy is described and it is shown how to represent the detected fiber trajectories using an efficient curve representation. The curve representation is then incorporated into an optimization framework to improve the initial estimate of the true fiber trajectories. Finally, the framework is evaluated on simulated data and on real tomography scans of a GFRP specimen.

1. Introduction

The development of advanced materials such as glass fiber-reinforced polymers (GFRP) is an essential part of materials science in the quest of making existing materials stronger and lighter [1]. To enable the development of materials with mechanical properties customized for their specific task, tools for the analysis and modeling of the composites are key. A popular choice for the analysis is the non-destructive testing using X-ray micro computed tomography (μCT). It is still an active research topic [2] and is approached through traditional image processing, as well as supervised and unsupervised Machine Learning to segment fibers, determine their locations, and analyze their direction distribution as well as to simulate tensile strength and suitability in different applications [3, 4, 5, 6, 7, 8].

Many of the GFRP analysis methods focus on a specific feature of the fiber composite, such as the orientation or length distribution of the fibers. Zauner et al. [9] use a template matching and binary thinning to extract fiber center lines and subsequently cluster the fibers in composites using tracing. This approach is elaborated by Bhattacharya et al. who introduced clustering on a fiber bundle level [10]. Emerson et al. [6] used semi-automatic Dictionary Learning (Insegt Fibre) to segment the fiber voxels from uni-directional GFRP samples and detect their centers per slice, stacking the resulting points on top of each other, subsequently clustering into individual fiber traces. While tracking individual fibers requires higher resolution than methods that extract parameter distributions, it provides the opportunity to extract various statistical measures without having to re-analyse the tomograms.

A compact parametric description of the fibers contained in a GFRP sample is convenient, as those models are easier to manipulate than a list of coordinates describing the center line and take significantly less memory to store than the voxel grids. Several ways of describing fibers as parametric curves in 3D space have been proposed. Adluru et al. use cosine series to represent and match long fiber traces from magnetic resonance imaging tractography data [11] and Lemkaddem et al. [12] employ splines for a similar purpose. Zhao et al. represent single fibers in yarn plies with circular helices [13]. The stress analysis following the extraction of the fibers is often carried out using either finite element analysis as a general purpose approach or mathematical models tailored to the application [7], for which a parametric representation could be used.

Parametric Reconstruction (PARE) is a theoretical framework for reconstructing individual straight glass fibers from tomographic reconstructions of GFRP samples and optimizing their orientation, location and length based on the projections used for the reconstruction [14]. It offers a convenient way to improve upon fiber traces by optimization directly in projection space. That is, PARE allows to retrieve fiber parameters, even if only few projections are available. The validity of the PARE framework has been shown on simulated data. Unfortunately, it has only been developed for perfectly straight fibers, and has not yet been demonstrated on real data.

In this work, a new framework called curved Parametric Reconstruction (cuPARE) is proposed. This method extends the fiber model to *curved* glass fibers and estimates the parameters of that model within a fully automatic processing pipeline from reconstructions from only a couple hundred projections. To that end, we use a parametric representation based on polynomials [15], able to accommodate for arbitrarily curved or deformed fiber trajectories while being compact and easy to manipulate. The fibers are clustered using a tracing based approach [16] and then optimized, reconstructing the parameters of the curve representation. Finally, a quality assessment of the retrieved fiber parameters on simulated and realistic data is calculated via a volumetric overlap metric and the estimated model is compared a model generated from traces detected by Insegt Fibre [6].

✉ tim.elberfeld@uantwerpen.be (T. Elberfeld); jan.sijbers@uantwerpen.be (J. Sijbers); jan.debeenhouwer@uantwerpen.be (J. De Beenhouwer)

ORCID(s): 0000-0002-0701-2421 (T. Elberfeld); 0000-0003-4225-2487 (J. Sijbers); 0000-0001-5253-1274 (J. De Beenhouwer)

2. Methods

Our proposed algorithm, cuPARE, consists of three stages. The first stage is the initial reconstruction of the volume from the tomograms and subsequent detection of the fibers within that reconstruction. In the second stage, the detected fiber voxels are clustered into individual fibers by means of tracing and then interpolated using polynomial curves, which serve as the concise fiber representation. This representation is converted into a mesh model to be projected. Finally, simulated CAD projections are optimized using the Nelder-Mead Simplex algorithm with a modification of the step parameters, that accommodate the high dimensional nature of the parameter space according to Gao et al. [17].

2.1. Fiber Center Line Detection

After reconstructing a 3D image from the acquired projections, the contained fiber voxels are detected. As prior knowledge we assume the radius of the fiber to be constant and known to the user. The fore- and background intensities, i.e. the intensity of the fiber voxels and the intensity of the polymer matrix voxels, respectively, are either known a priori (e.g., in the case of simulations), or estimated from the histogram.

To extract the fiber voxels, the polymer matrix is first removed using the h-dome transform [18]. This morphological transform, based on morphological reconstruction, suppresses the background of an image while preserving the foreground. After this step, values below a threshold t, a percentage of the maximum intensity, were set to zero. The threshold was set to 60% of the maximum intensity in this work, but is a user parameter that can be adjusted depending on the contrast in the reconstruction. Following this, a template matching using a spherical template with the mean fiber radius [19] is computed. The template matching image has maxima at the center lines of the fibers in the volume. Those center lines are then extracted using the same threshold as before, this time setting the foreground to 1 and the background to 0. This method might produce hollow tubes in some cases. To remove the holes a binary closing is applied to solidify the binary objects. Finally, the center lines are obtained from the resulting binary image using binary thinning or skeletonization [20]. Cross connections that still remain after this are removed by removing all voxels that have 3 or more nonzero neighbors [21].

2.2. Parametric Fiber Representation

The polynomial representation of the fibers consists of three 2D curves g_x, g_y, g_z which together describe the x, y, and z coordinates of the center line. Given the traced points of the fiber center line, a least-squares curve is computed, parameterized in terms of the locus on the fiber center line $u \in [0, 1]$. This results in the following representation of the fiber from its 3D coordinates

$$g(u) = \begin{pmatrix} g_x(u) \\ g_y(u) \\ g_z(u) \end{pmatrix} = \begin{pmatrix} \sum_{j=0}^{k} a_{x_j} u^j \\ \sum_{j=0}^{k} a_{y_j} u^j \\ \sum_{j=0}^{k} a_{z_j} u^j \end{pmatrix}, \qquad (1)$$

with k the degree of the used polynomials. Thus a single fiber can be represented completely using $3(k+1)$ parameters combined in a list ξ_i, independent of its length or curvature.

$$\xi_j = \begin{pmatrix} a_{x_0}^{(j)}, a_{x_1}^{(j)}, \ldots, a_{x_k}^{(j)} \\ a_{y_0}^{(j)}, a_{y_1}^{(j)}, \ldots, a_{y_k}^{(j)} \\ a_{z_0}^{(j)}, a_{z_1}^{(j)}, \ldots, a_{z_k}^{(j)} \end{pmatrix} \forall \xi_j \in \Xi \qquad (2)$$

with Ξ the set of all fiber parameter lists of the fibers detected in $\mathbf{x}$. Using this representation, the optimization can be performed, improving upon the initial center line estimate made by the tracing algorithm. An example of such a curve in 3d space and the resulting mesh model, that is used to project the estimated fiber, is shown in Figure 1. It is convenient to define the notion of a fiber object, based on the parameter list as well. Let

$$Z = \{\zeta_1, \zeta_2, \ldots, \zeta_N\} = \bigcup_{\xi_i \in \Xi} \{\text{fib}(\xi_i, r)\} \qquad (3)$$

be the set of all fiber objects and $\text{fib}(\bullet)$ a function that converts a fiber parameter list ξ_j and a radius r to a fiber object ζ_j.

2.3. Fiber Tracing

Using the skeletonized fiber centers, the tracing [16] is started with all fiber center line coordinates as so called seed points. Additionally, the local direction in each voxel is computed. The direction is obtained from the the Eigenvectors of the Hessian matrix of the reconstruction $\mathbf{x}$, convolved with a Gaussian g_σ with standard deviation equal to the fiber radius $H_\sigma = (\nabla\nabla)^T(\mathbf{x} * g_\sigma)$. The direction of lowest curvature, i.e. the local direction of the fiber, is the Eigenvector corresponding to the Eigenvalue with the smallest magnitude [22].

Until all seed points have been marked as 'visited', the following process is repeated. A fiber is considered as a collection of connected straight segments. Each segment is a cylinder with the fiber radius and height of 2.5 times the fiber radius. The initial segment of a fiber is created at a random seed point. The cylinder axis is the local direction in that voxel. As the direction information from the Hessian often deviates significantly from the direction of the center line, the seed points within the axis aligned bounding box of the initial cylinder segment are then used to estimate a new direction by means of a least-squares fit of the seed coordinates. All seed points used for the fit are marked as visited. The next segment is centered around the closest seed point to the previous cylinder segment that has not yet been visited. The segment is added to the fiber if it meets the following requirements:

1. the smallest distance L between the segments is smaller than $d_{\max}$

Figure 1: (a) Curve representing a fiber in 3d space and the voxels it was estimated from. A wire frame around the curve is shown to visualize the triangle mesh model of the fiber that is used in the end to represent the fiber for generating projections. (b) shows a close up of a part of the voxels (red and blue), center line (dark green) and the wire frame (black) is partially cut to reveal the voxels and center line.
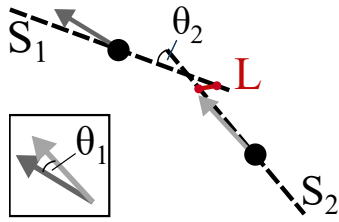

Figure 2: Schematic of two straight segments S_1 and S_2 as they can appear during the tracing procedure and how the angles θ_1, the angle between the direction vectors and θ_2, the angle between the segments as well as the distance between the segments L are computed.

2. the angle θ_1 between the the direction vector at the center of the new segment and the estimated direction vector at the center of the current segment needs to be smaller than α_1.

3. the angle θ_2 between the current segment's axis and the new segment's axis needs to be smaller than α_2.

A schematic of how the criteria are applied to two segments is shown in Figure 2

For the experiments in section 3, $\alpha_1 = 20°$, $\alpha_2 = 20°$, $d_{\min} = r_{\text{fiber}}$ and $d_{\max} = 3r_{\text{fiber}}$ were used, which has been empirically chosen and proven to be adequate for the datasets investigated so far. If the above conditions are met, the segment is added to the fiber. Otherwise, if the tracing went into the direction of the cylinder axis, the tracing restarts at the first segment, in the opposite direction until it stops there as well.

The spherical template causes regions at either end of the fiber to differ from the rest of the fiber. Thus, the fibers are estimated systematically too short by a value roughly equal to the fiber radius when applying the threshold. To counteract this, the detection is finalized with an end point detection step. To obtain the fiber edges, a line is sampled along the first and last segment of the fiber and the intensities in the original reconstructions are recorded at those lines. The resulting line profiles are then interpolated using splines and the largest intensity step is found by evaluating the first and second derivatives of the splines [14]. An additional line segment is added between the previous end point and the newly detected end point. In case of low contrast, the end detection is rejected and the original fiber end is kept, as the detection is unreliable otherwise. The threshold for this rejection is 85% of the range between attenuation values for polymer matrix and fibers. If the contrast is higher than that, the detection is considered reliable.

2.4. Projecting the Fibers

In our previous work [14], fiber voxel models were generated from their parameters and subsequently projected using the ASTRA toolbox [23]. This requires expensive computations both for generating and projecting the voxel model. In this work, a triangle mesh/CAD model using VTKs tube filter [24] on the detected fiber center lines is generated. To achieve realistic borders, the tube model is then cut off at the volume boundary if it is protruding out of it using a Boolean intersection [25] of the fiber mesh and a cube representing the volume. The resulting fiber mesh is projected using a custom, GPU accelerated, CAD projector [26]. This reduces the computational load significantly. Additionally, the projection data used for the computation of the objective function is cropped to reduce the amount of data needed to be generated and transferred to and from the GPU. To that end, the axis aligned bounding box of the current fiber being optimized is computed in reconstruction space. This bounding box is then projected onto the detector for each projection angle and the largest overlapping region of all projected bounding boxes is computed. Finally, the region is extended in its largest dimension to span the whole width or height of the detector. This can reduce the amount of pixels significantly, depending on the orientation and position of the fiber relative to the rotation axis of the tomography setup.

2.5. Fiber Optimization

The Nelder-Mead Simplex algorithm is used for the optimization of the fibers in projection space, i.e. using only the projections used for the reconstruction of the volume or a subset thereof. To keep the fiber parameter space as low dimensional as possible, each individual fiber is optimized

separately. Thus, for a single fiber parameter set the optimization problem becomes

$$\hat{\xi}_j = \arg \min_{\xi_j \in \mathbb{R}^{3(k+1)}} f_{\text{loss}}(\mathbf{p}, \mathbf{W}\mathbf{x}(\xi_j)) \quad , \qquad (4)$$

where f_{loss} is some objective function, k is the degree of the polynomials representing the fiber center line, $\mathbf{p}$ the measured projection data and $\mathbf{W}\mathbf{x}$ the forward projection of an estimate of the reconstruction as a function of the fiber parameter list ξ_i.

The parameter values are converted to be in the range of $[0, 1]$ while they are manipulated during optimization, leading to better numerical stability. To convert to the normalized range, the whole population of estimated fibers is considered. The conversion is therefore mapping 0 to the lowest value that each coefficient had in the population and 1 to the highest value in each coefficient. This keeps the step-size the same for each parameter, even when the parameters have vastly different ranges originally. Once a fiber needs to be generated, the values are converted back to their original range.

With the more complex fiber model, the objective function is increasingly complex as well. The mean of the sum of the squared projection differences or root mean squared error (RMSE) is notoriously sensitive to slight differences in intensity. As the main objective is to estimate the fiber shape the SSIM Loss [27]

$$\text{SSIM}_{\text{loss}}(\mathbf{A}, \mathbf{B}) = \frac{1}{2}\left(1 - \frac{1}{M}\sum_{i=1}^{M}\text{SSIM}(\mathbf{a}_i, \mathbf{b}_i)\right) \quad (5)$$

$$= \frac{1}{2}\left(1 - \text{MSSIM}(\mathbf{A}, \mathbf{B})\right).$$

was chosen as the objective function for the optimization. The SSIM measure is computed on M local windows $\mathbf{a}_i$ and $\mathbf{b}_i$, which are corresponding regions in the projections $\mathbf{A}$ and $\mathbf{B}$ and then averaged resulting in a scalar measure. This measure is widely used in Deep Learning in combination with the RMSE to tackle similar problems in image similarity assessment and has proven to be much more robust as a measure than the RMSE in our experiments. To compensate for noisy projections the projections can be smoothed per projection view with a Gaussian filter of variable width, depending on the noise level of the input images.

2.6. Assessment of optimization quality

For datasets with the ground truth or a reference dataset available, the quality of the optimization with respect to the fiber morphology can be verified. This was done by means of a volumetric overlap metric introduced in [28]

$$d_3^o(a, b) = 1 - o(a, b)\begin{cases} \frac{\nu(a)}{\nu(b)} & \text{if } \nu(a) < \nu(b) \\ \frac{\nu(b)}{\nu(a)} & \text{otherwise} \end{cases}, \qquad (6)$$

where $o(a, b)$ denotes the volumetric overlap of two fibers a and b and $\nu(\bullet)$ denotes the volume of a fiber. The volumetric

overlap of a and b is defined as the number n of points sampled within the volume of fiber a that are contained in fiber b divided by the total number of sampled points N. A value of 0 denotes that the two fibers are identical, whereas a value of 1 would show that no common partial volume between them exists. In Section 4 the term *overlap dissimilarity* will be used synonymous to d_o^3, but will be emphasized to make this clear. The *overlap dissimilarity* is also used to obtain a mapping from the ground truth fiber set Z_{gt} to the estimated fibers Z_{est}, so the corresponding fibers in both sets can be identified

$$m : Z_{\text{gt}} \to Z_{\text{est}} \qquad (7)$$
$$\zeta_j \mapsto \arg\min_{\zeta_i \in Z_{\text{est}}} d_o^3(\zeta_j, \zeta_i).$$

Using an overlap based metric is important here, as fibers that are too short, but contained in a larger fiber of the ground truth, are often further from the ground truth in parameter space than fibers located next to each other, running parallel. A simple comparison of the parameters is therefore worse at estimating fibers that correspond between the two sets.

3. Experiments

To validate our method, the tracing and optimization was performed on two simulated datasets, subsequently named *SimA* and *SimB*, containing a mixture of curved and straight fibers, varying fiber radii and exhibiting two different noise levels.

The cuPARE algorithm was then applied to a realistic, publicly available, dataset of unidirectional glass fibers embedded in a polymer resin [29] (XCT_H). As a comparison to the previous method the detected fiber center lines were also interpolated using polynomials with $k = 1$, to emulate using PARE instead of cuPARE.

For the optimization of the simulated datasets the stop condition for the optimization was either after 1000 iterations, or if the simplex vertex with the best and the simplex vertex with the worst value in f_{loss} had at most a difference of 1×10^{-5}. The iteration limit for dataset XCT_H was also 1000, but the error delta was slightly higher with 5×10^{-4}.

3.1. Experiment 1: Simulation

The fiber composite phantoms were simulated consisting of a polymer matrix and glass fibers just as in [14]. The RSA algorithm was used to position fiber shapes into a volume in random orientations following a von Mises-Fisher distribution in $\mathbb{R}^3$.

$$\text{VMF}(\mathbf{x}; \mu, \kappa) = \frac{\kappa}{2\pi(e^\kappa - e^{-\kappa})}\exp(\kappa\mu^{\text{T}}\mathbf{x}), \qquad (8)$$

with the mean direction $\mu = (1, 0, 0)$.

The curved fibers were generated by choosing three points on a straight line, following the orientation drawn from the direction distribution. The central point was then displaced by a random amount within the plane perpendicular to the fiber axis and a parabola was fitted through
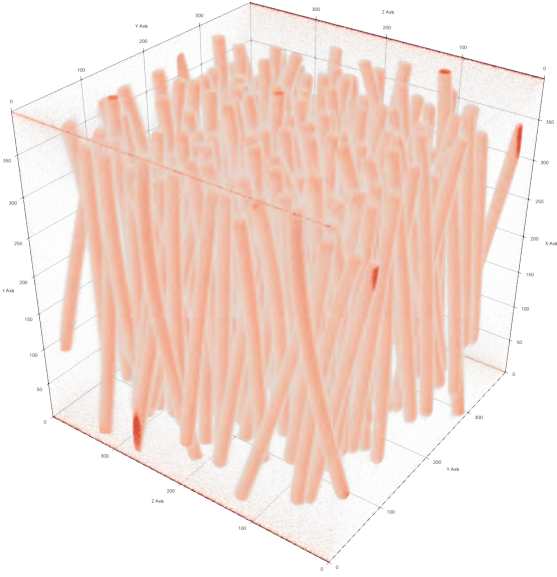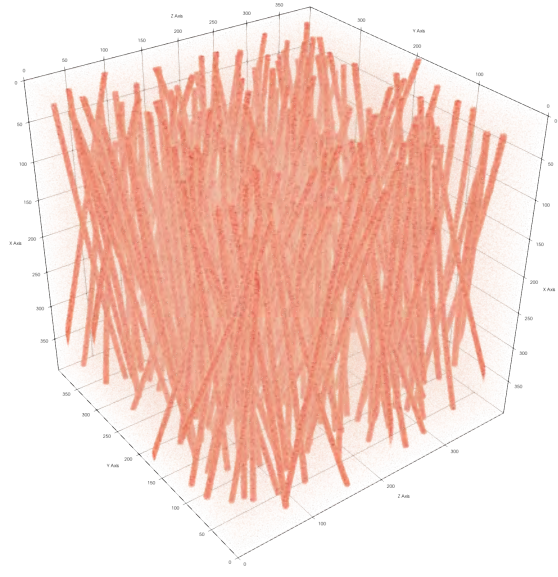
(a) Reconstruction of *SimA*

(b) Reconstruction of *SimB*

Figure 3: Reconstructions with $400 \times 400 \times 400$ voxels of the simulated datasets. The reconstruction was performed using 100 iterations of the Barzilai-Borwein [30] algorithm and the background was made transparent to make the fibers more visible.

the three points, generating the final centerline of the fiber. This displacement, influencing the amount of curvature, was randomly chosen from the interval [6, 14] voxels for *SimA* and [3, 7] voxels for *SimB*.

The first simulated dataset, *SimA*, is shown in Figure 3a. Here 186 fibers were added to a volume of size $400 \times 400 \times 400$ with varying degrees of curvature. The fiber radius was 6.5 ± 0.3 voxels, simulating slight variations in the fiber production process. The spread parameter κ_A was arbitrarily set to 50, modeling nearly uni-directional fibers. The second dataset, *SimB*, has the same voxel dimension, but contains 225 fibers with a smaller radius of 4.0 ± 0.3 voxels and the fiber directions are spread wider, with κ_B being set to 26. This second dataset is visualized in Figure 3b. In both datasets the length of the fibers was set to 340 ± 40 voxels to generate fibers that are fully included in the volume, as well as fibers that are cut by the volume borders on one end or on both.

The projection geometry for both simulated datasets was modeled after the scanner setup in our laboratory [31]. The source-object-distance (SOD) was 19.9 mm and the source-detector-distance (SDD) 1995.0 mm, with a voxel size of 3 μm and a 1024×1024 detector with a pixel size of 150 μm. With this geometry 100 projections equidistant on the full circle were simulated. Poisson noise was added to the projections, simulating 10000 photons per detector pixel in the first dataset and 12000 photons per pixel in the second dataset. Additionally an intensity drop-off of from the center due to the X-rays hitting the detector at an oblique angle as well as the increased distance due to the flatness of the detector was simulated. A slight correlation between the detector pixels (i.e. a point spread function) using a Gaussian filter with width $\sigma = 0.3$ voxels was also applied.

The peak-signal-to-noise-ratio (PSNR)

$$\text{PSNR} = 10 \log_{10} \left(\frac{\max(p_{\text{gt}})}{\text{MSE}(p_{\text{gt}}, p_{\text{noisy}})} \right)$$

of the simulated projections was 42.63 dB and 43.62 dB for *SimA* and *SimB*, respectively. Here p_{gt} is the noiseless projection and p_{noisy} the projection with added Poisson noise. The function $\text{MSE}(\bullet)$ denotes the mean squared error and max the maximum value of the input.

3.2. Experiment 2: Unidirectional GFRP

Our method was also applied to a publicly available dataset of high resolution scans of a uni-direcional glass fiber-reinforced polymer sample reconstructed from 4201 projections [29]. To obtain the projection data, an experiment was simulated using the reconstruction as a phantom. To reduce processing time, a $256 \times 256 \times 256$ cutout of the high resolution X-ray CT dataset (XCT_{H} [29]), containing 209 individual fibers, was extracted from the larger reconstructed volume. Figure 4 shows the cutout that was used in this experiment. The intensity of the polymer matrix was estimated at 0.04 ± 0.02 and the intensity of the fibers was estimated at 0.608 ± 0.22. The projection data for the optimization was composed of only 100 projections on the full circle. The geometry to simulate those projections was defined with an SDD of 55.0027 mm and an SOD of 10.0141 mm. To achieve good coverage of the projections on the detector, the voxel size was set to 1 μm and the pixel size of the 1024×1024 detector was 2 μm. This reduces the effective pixel size to 0.36μm, giving a subsampling effect. This does not affect the projection of the voxel based reconstruction, as the voxel size is fixed in the ASTRA toolbox. The subsampling does, however, affect the projections of the mesh
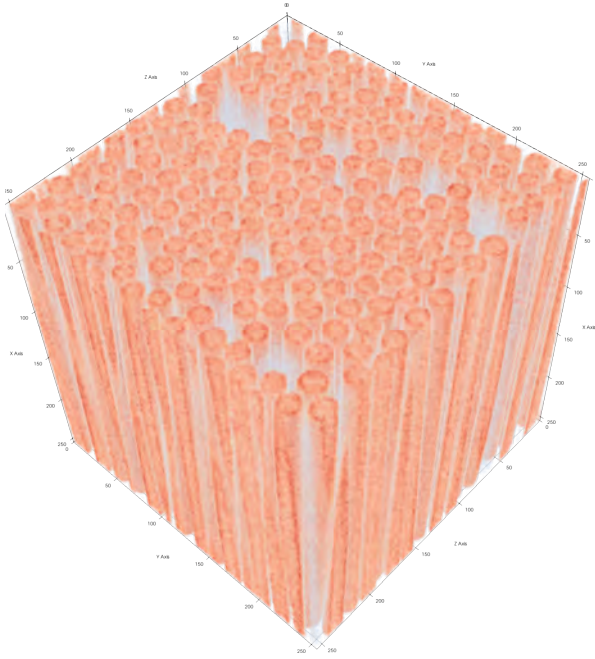
Figure 4: Cutout of a small region of $256 \times 256 \times 256$ voxels from the high resolution dataset from [29] used as a realistic phantom. The polymer matrix was made transparent to make the fibers more visible.

Figure 5: Boxplot of the *overlap* scores for each fiber in *SimA* before and after optimization. (a) and (b) show d_o^3 for the detected and optimized fibers with $k = 1$, which is equivalent to using PARE. (c) and (d) show the same for $k = 3$, showing the algorithm cuPARE. The median of each boxplot is written out on the top and matches the color of the line in the plot.

model by that amount when projecting during optimization, because the model is defined by its vertices, whose position in space is defined with floating point precision.

4. Results

For the first simulation experiment, all fibers were detected and thus each fiber was optimized as well. Using the previously described *overlap dissimilarity* metric, the quality of the fit both before and after the optimization can be assessed. Figure 5 shows boxplots of the *overlap dissimilarity* for *SimA*. It is clear that the median *overlap dissimilarity* score improves significantly with optimization, being reduced from 0.0685 to 0.0089. This means that over 99% of the total volume overlaps after the optimization. To compare these results to PARE, the tracing and optimization was performed a second time, this time reducing the degree of the polynomials to $k = 1$ to simulate only being able to analyze straight fibers. As expected, the *overlap dissimilarity* was lower than for the polynomial interpolation with a higher degree. Before the optimization the median *overlap dissimilarity* was 0.1645, while it dropped to 0.1475 after optimization. Note that here the *overlap dissimilarity* never reaches the value 0, as the fibers can never exactly overlap when using linear functions, whereas with cuPARE the shape can be fully matched.

Similarly the *SimB*, which contained 225 fibers, was analyzed. Due to the smaller fiber diameter used in this dataset, the detection is slightly erroneous and 226 fibers are detected. Several fibers were not completely detected and some were split into two segments during the tracing,
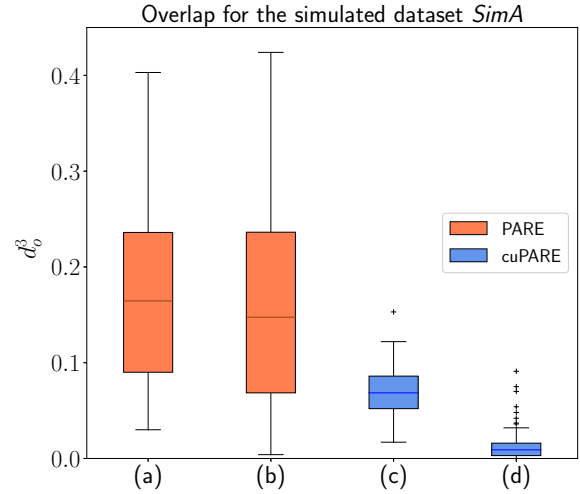
causing this discrepancy. The individual pieces can be optimized separately and overlap at the end of the optimization, forming a full fiber. This effect can be seen in Figures 9g and 9h when comparing the difference image before and after optimization. Some of the fibers that do show up as positive values disappear, while others stay. The former are fibers split into segments, which individually settle in their correct locations, the latter are fibers that are too short and can not be improved by the optimization.

The median *overlap dissimilarity* for *SimB* was 0.073 and was decreased to 0.033 after the optimization with the cuPARE parameters. Using PARE, the median *overlap dissimilarity* was 0.164 after detection, improving to 0.143 after optimization. Again it is clear that the results are much better when using higher degree polynomials, as the fibers are curved. The curvature of the fibers in *SimB* is much lower, however, so the results are generally better than for fibers with a higher curvature. This also means that the optimization works better in this case. The complete *overlap dissimilarity* results are shown as boxplots in Figure 6.

In addition to the boxplots, a visualization of the differences between the sets of detected and optimized fibers compared to the ground truth is shown in Figure 9 for both simulated datasets. This figure also includes the SSIM and MSE of two fiber sets. To calculate those measures both fiber sets were rendered into a voxel volume of the same size as the original reconstruction where the background was 0 and the fiber objects were set to 1. The SSIM and MSE was then computed for the image pairs.

For the dataset shown in Figure 4 traces in the form of sequences of coordinates were available from Insegt Fibre, so the *overlap dissimilarity* between our results and the results they obtained can be computed. Of the 209 fibers
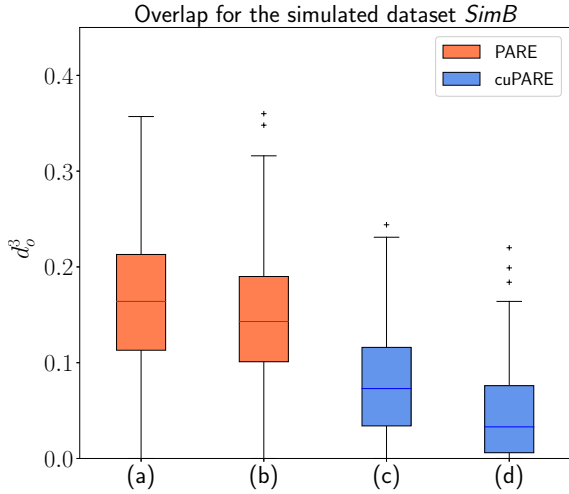
Figure 6: Boxplot of the *overlap* scores for each fiber in *SimB* before and after optimization. (a) and (b) show d_o^3 for the detected and optimized fibers with $k = 1$, which is equivalent to using PARE. (c) and (d) show the same for $k = 3$, showing the algorithm cuPARE. The median of each boxplot is written out on the top and matches the color of the line in the plot.

that were contained in the volume most were detected. The tracing found 221 traces, of which some are the result of a fiber splitting during tracing. The fibers that were not detected at all were partially cut off and thus did not have enough information within the actual volume to be traced properly. The median *overlap dissimilarity* of the detected fibers with the results from Insegt Fibre initially was 0.097 and was lowered by optimization to 0.074. The boxplots of the *overlap dissimilarity* of the detection and subsequent optimization relative to the available traces are shown in Figure 8 and a difference image of the two fiber sets from those boxplots are shown in Figure 7.

Figures 10 and 11 show the arclength distribution and orientation distributions of the datasets analyzed with PARE and cuPARE. The arclength is the length of the fiber along the curve or the distance of start and end point for straight fibers. For the orientation distribution visualization the normalized direction vector of the least square line of all points on the curve was converted to spherical coordinates and the azimuth angle φ was projected onto the disk by computing $r\cos(\varphi)$, so the coordinates of each orientation vector could be expressed in polar coordinates.

It is clear that for the simulated datasets the orientation distributions can be retrieved using PARE and cuPARE when optimizing, the detection alone being slightly off in estimating fiber length, biased towards higher values. For the realistic dataset the lengths could not be matched exactly, but optimization improves the length estimates. The fiber orientation is very close both in the simple detection of the fibers as well as after optimization, relative to the traces obtained with InsegtFibre.

5. Discussion and Future Work

The cuPARE algorithm presented in this work is able to detect curved as well as straight fibers in simulated and realistic data and create a mathematical model of the individual fibers in those datasets. It was shown that it is possible to estimate the shape of those individual fibers based on relatively few projections.

Slight mistakes in the fiber tracing can be compensated through the optimization. This is especially apparent when looking at the length distributions of the simulated fibers before and after optimization. However, large differences in fiber morphology can cause the optimization procedure to converge to local minima. The method is not limited to the analysis pipeline proposed here. Different methods of detecting the fibers and representing them with parametric models can be employed and improved upon using the measured projection information. The method is not even limited to fibers; the detection and geometric model can be adjusted to reflect any shape, as long as optimization is possible with a reasonable parameter space, as a high dimensional parameter space makes the optimization more difficult.

The procedure to simulate projections from the models could still be improved. For now, the CAD projector uses meshes generated from the center line, but those do not depend on the line continuously. The tube filter generating the model can produce jumps in the objective function for small variations, which decreases numerical stability of any optimization procedure. Additionally, noise in the projections disturbs the SSIM measure on a small scale, which is partially compensated with smoothing, but reduces the overall achievable accuracy.

Ideally, the projector should be able to produce a projection image from the coefficients of the center line directly. A signed-distance-function based approach could work here, as it continuously defines the surface of the fiber. However, this would require a tailor made projector for such objects, which is currently not available to the author's knowledge.

Another possible solution would be to compute analytic derivatives per vertex of the fiber mesh and then move those vertices accordingly, enabling a smooth transition between two fibers that are close in parameter space. Koo et al. [32] lay the groundwork for such an approach and Renders et al. [33] already apply a similar method to 4D-CT images of foam.

Finally, as future work we aim to include more parameters into the model, such as the radius of the fiber or a combination of fibers with different materials. Extending the model to woven fiber bundles [34] will also be considered, as well as a mixture of different objects, e.g. modeling pores and inclusions in addition to fibers.

To do (1) **To do** (2)
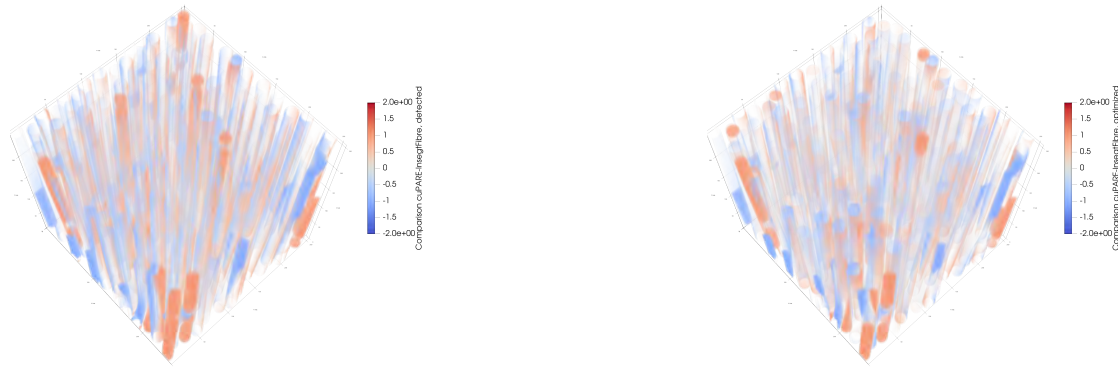
(a) Comparison with **InsegtFibre**, **cuPARE**, **detected**, SSIM = 0.687, MSE = 0.083

(b) Comparison with **InsegtFibre**, **cuPARE**, **optimized**, SSIM = 0.773, MSE = 0.055

Figure 7: Difference images of the fiber models of both Insegt Fibre and cuPARE traces before and after optimization of the fibers detected with cuPARE.
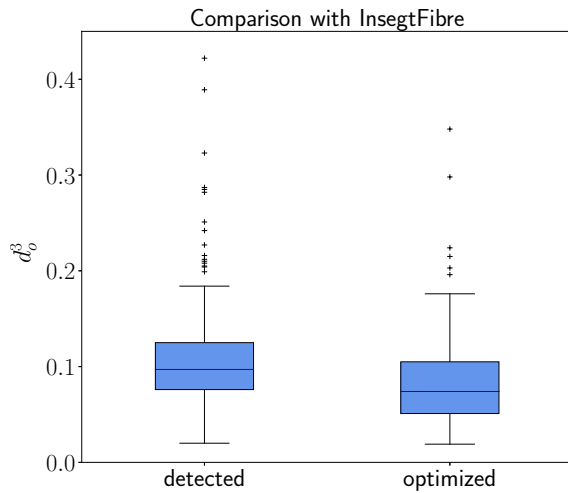

Figure 8: Boxplot of the *overlap dissimilarity* scores for each fiber in the realistic dataset containing unidirectional fibers.

Acknowledgements

References

[1] F. T. Wallenberger, J. C. Watson, H. Li, Glass fibers, in: ASM Handbook: Composites, volume 21, ASM International, 2001, pp. 27–34.

[2] S. Garcea, Y. Wang, P. Withers, X-ray computed tomography of polymer composites, Composites Science and Technology 156 (2018) 305–319.

[3] F. Sket, A. Enfedaque, C. Alton, C. González, J. M. Molina-Aldareguia, J. Llorca, Automatic quantification of matrix cracking and fiber rotation by X-ray computed tomography in shear-deformed carbon fiber-reinforced laminates, Composites Science and Technology 90 (2014) 129–138.

[4] T. K. Konopczynski, D. Rathore, J. Rathore, T. Kröger, L. Zheng, C. S. Garbe, S. Carmignato, J. Hesser, Fully convolutional deep network architectures for automatic short glass fiber semantic segmentation from CT scans, in: 8th Conference on Industrial Computed Tomography (iCT), 2018.

[5] T. Baranowski, D. Dobrovolskij, K. Dremel, A. Hölzing, G. Lohfink, K. Schladitz, S. Zabler, Local fiber orientation from X-ray region-of-interest computed tomography of large fiber reinforced composite components, Composites Science and Technology 183 (2019) 107786.

[6] M. Emerson, A. Dahl, K. Conradsen, V. Dahl, Insegt fibre: A user-friendly software for individual fibre segmentation, in: 22nd International Conference on Composite Materials (ICCM22), 2019.

[7] A. Bhattacharjee, H. Roy, Assessment of tensile and damping behaviour of hybrid particle/woven fibre/polymer composites, Composite Structures 244 (2020) 112231.

[8] J. S. Rathore, T. Konopczyński, J. Hesser, G. Lucchetta, S. Carmignato, Investigation on Tomographic-Based Nondestructive Characterization of Short Glass Fiber-Reinforced Composites as Obtained From Micro Injection Molding, Journal of Nondestructive Evaluation, Diagnostics and Prognostics of Engineering Systems 3 (2020).

[9] H. Zauner, D. Salaberger, C. Heinzl, J. Kastner, 3d image processing for single fibre characterization by means of xct, Proceedings of the 14th International Congress for Stereology and Image Analysis - Acta Stereologica (2015).

[10] A. Bhattacharya, C. Heinzl, A. Amirkhanov, J. Kastner, R. Wenger, MetaTracts - A method for robust extraction and visualization of carbon fiber bundles in fiber reinforced composites, in: 2015 IEEE Pacific Visualization Symposium (Pacific Vis), 2015, pp. 191–198.

[11] N. Adluru, A. L. Alexander, M. K. Chung, J. E. Lainhart, M. Lazar, J. E. Lee, Cosine series representation of 3D curves and its application to white matter fiber bundles in diffusion tensor imaging, Statistics and Its Interface 3 (2010) 69–80.

[12] A. Lemkaddem, D. Skiöldebrand, A. Dal Palú, J.-P. Thiran, A. Daducci, Global tractography with embedded anatomical priors for quantitative connectivity analysis, Frontiers in Neurology 5 (2014) 232.

[13] S. Zhao, F. Luan, K. Bala, Fitting procedural yarn models for realistic cloth rendering, ACM Trans. Graph. 35 (2016).

[14] T. Elberfeld, J. De Beenhouwer, A. den Dekker, C. Heinzl, J. Sijbers, Parametric reconstruction of glass fiber-reinforced polymer composites from x-ray projection data - a simulation study, Journal of Nondestructive Evaluation 37 (2018).

[15] T. Elberfeld, B. Fröhler, M. J. Emerson, C. Heinzl, J. Kastner, J. De Beenhouwer, J. Sijbers, Efficient parametric curved glass fiber representations, in: 20th World Conference on Non-Destructive Testing
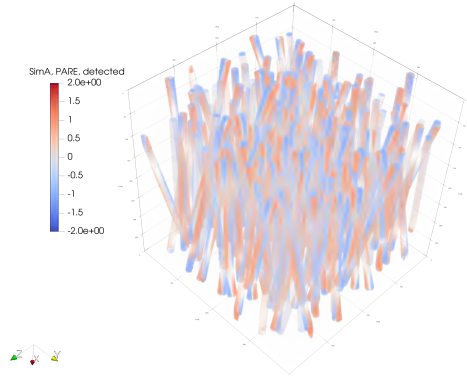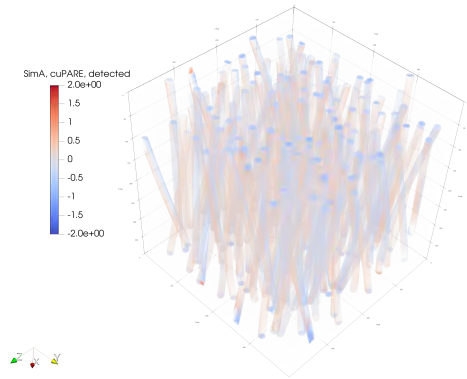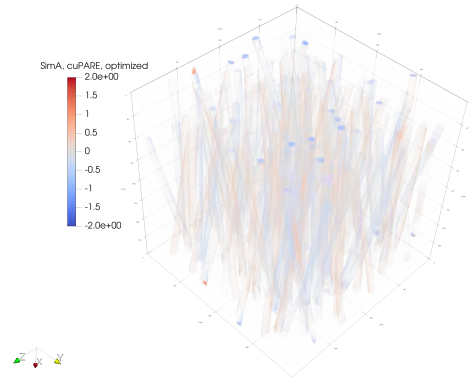
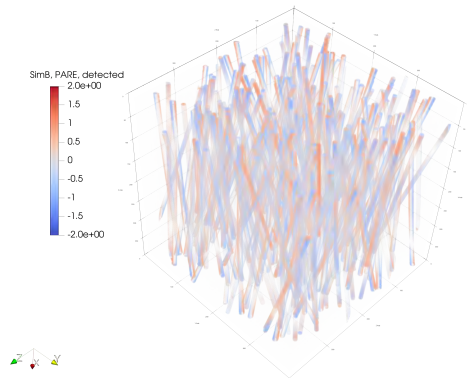(a) *SimA*: **PARE, detected**, SSIM = 0.824, MSE = 0.031
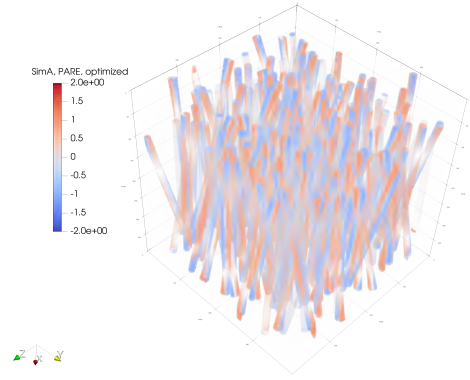
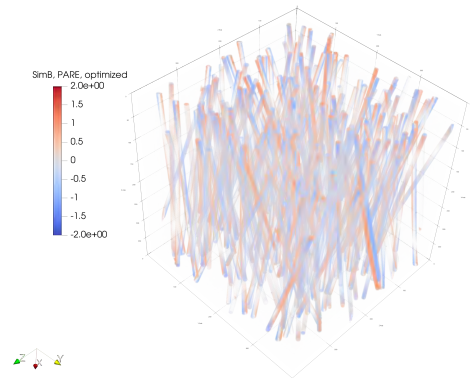(b) *SimA*: **PARE, optimized**, SSIM = 0.824, MSE = 0.032

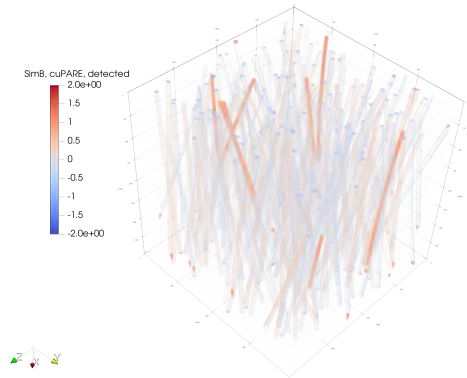(c) *SimA*: **cuPARE, detected**, SSIM = 0.921, MSE = 0.008.

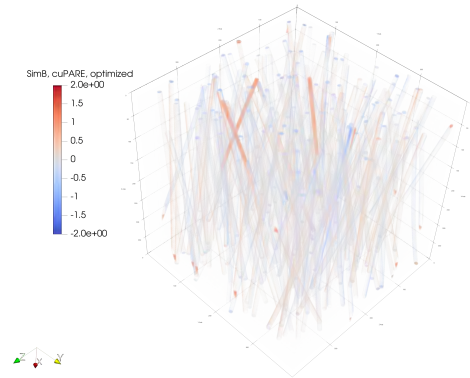(d) *SimA*: **cuPARE, optimized**, SSIM = 0.968, MSE = 0.002.

(e) *SimB*: **PARE, detected**, SSIM = 0.901, MSE = 0.012.

(f) *SimB*: **PARE, optimized**, SSIM = 0.900, MSE = 0.012.

(g) *SimB*: **cuPARE detected**, SSIM = 0.958, MSE = 0.004.

(h) *SimB*: **cuPARE, optimized**, SSIM = 0.970, MSE = 0.002.

Figure 9: Overview of the detection (left column, 9a, 9c, 9e, 9g) and optimization (right column, 9b, 9d, 9f, 9h) of the simulated datasets. Each image shows the difference of the ground truth and the detected and optimized fibers rendered into a voxel grid of the same size as the reconstruction.
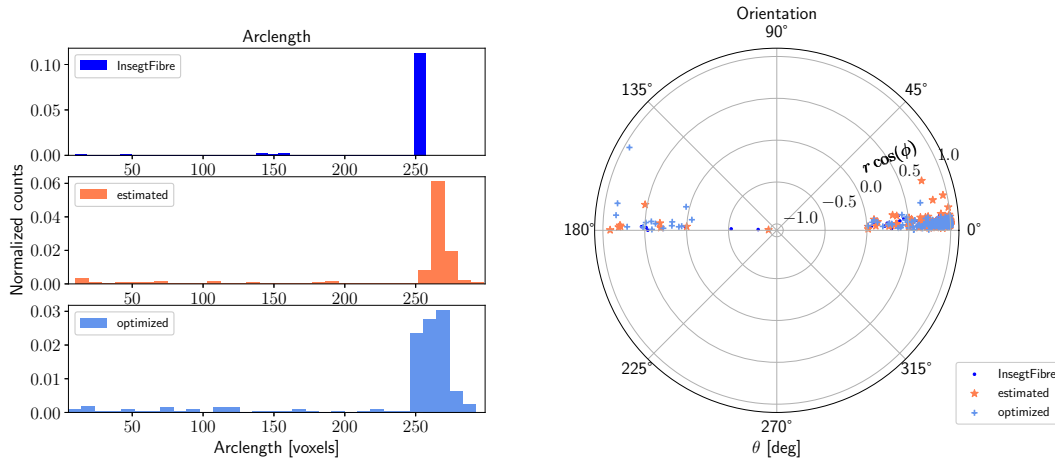
Figure 10: Length and orientation distribution of the traces from InsegtFibre, estimated and optimized using cuPARE.

(WCNDT), 2020. Accepted.

[16] T. Elberfeld, J. De Beenhouwer, J. Sijbers, Fiber assignment by continuous tracking for parametric fiber reinforced polymer reconstruction, in: Proc. SPIE 11072, 15th International Meeting on Fully Three-Dimensional Image Reconstruction in Radiology and Nuclear Medicine, 2019. doi:10.1117/12.2534836.

[17] F. Gao, L. Han, Implementing the Nelder-Mead simplex algorithm with adaptive parameters, Computational Optimization and Applications 51 (2012) 259–277.

[18] C. P. Schwegmann, W. Kleynhans, B. P. Salmon, L. Mdakane, Ship detection in sentinel-1 imagery using the h-dome transformation, in: 2015 IEEE International Geoscience and Remote Sensing Symposium (IGARSS), 2015, pp. 3711–3714. doi:10.1109/IGARSS.2015.7326629.

[19] J. P. Lewis, Fast Template Matching, Vision Interface 95 (1995) 120–123.

[20] T.-C. Lee, R. Kashyap, C.-N. Chu, Building skeleton models via 3-d medial surface/axis thinning algorithms, CVGIP Graph. Model. Image Process. 56 (1994) 462–478.

[21] D. Salaberger, Micro-structure of discontinuous fibre polymer matrix composites determined by X-ray computed tomography, Ph.D. thesis, TU Wien, 2019.

[22] O. Wirjadi, K. Schladitz, P. Easwaran, J. Ohser, Estimating fibre direction distributions of reinforced composites from tomographic images, Image Analysis & Stereology 35 (2016) 167–179.

[23] W. van Aarle, W. J. Palenstijn, J. Cant, E. Janssens, F. Bleichrodt, A. Dabravolski, J. De Beenhouwer, K. J. Batenburg, J. Sijbers, Fast and flexible x-ray tomography using the astra toolbox, Opt. Express 24 (2016) 25129–25147.

[24] W. Schroeder, K. Martin, B. Lorensen, The visualization toolkit (4th ed.), Kitware (2006).

[25] Q. Zhou, Pymesh, 2021. URL: https://github.com/PyMesh/PyMesh, retrieved 2021-10-12.

[26] Á. Marinovszki, J. D. Beenhouwer, J. Sijbers, An efficient CAD projector for X-ray projection based 3D inspection with the ASTRA Toolbox, in: 8th Conference on Industrial Computed Tomography, Wels, Austria, 2018.

[27] Z. Wang, A. Bovik, H. Sheikh, E. Simoncelli, Image quality assessment: from error visibility to structural similarity, IEEE Transactions on Image Processing 13 (2004) 600–612.

[28] B. Fröhler, T. Elberfeld, T. Möller, H.-C. Hege, J. De Beenhouwer, J. Sijbers, J. Kastner, C. Heinzl, Analysis and comparison of algorithms for the tomographic reconstruction of curved fibres, Nondestructive Testing and Evaluation 35 (2020) 328–341.

[29] M. J. Emerson, V. A. Dahl, K. Conradsen, L. P. Mikkelsen, A. B. Dahl, A multimodal data-set of a unidirectional glass fibre reinforced polymer composite, Data in Brief 18 (2018) 1388–1393.

[30] J. Barzilai, J. M. Borwein, Two-Point Step Size Gradient Methods, IMA Journal of Numerical Analysis 8 (1988) 141–148.

[31] B. D. Samber, J. Renders, T. Elberfeld, Y. Maris, J. Sanctorum, N. Six, Z. Liang, J. De Beenhouwer, J. Sijbers, FleXCT: a Flexible X-ray CT scanner with 10 degrees of freedom, Optics Express 29 (2021) 3438–3457.

[32] J. Koo, A. B. Dahl, J. A. Bærentzen, Q. Chen, S. Bals, V. A. Dahl, Shape from projections via differentiable forward projector for computed tomography, Ultramicroscopy 224 (2021) 113239.

[33] J. Renders, J. D. Beenhouwer, J. Sijbers, Mesh-based reconstruction of dynamic foam images using x-ray ct, in: International Conference on 3D Vision (3DV2021), 2021.

[34] Y. Sinchuk, P. Kibleur, J. Aelterman, M. Boone, W. Paepegem, Geometrical and deep learning approaches for instance segmentation of CFRP fiber bundles in textile composites, Composite Structures 277 (2021).
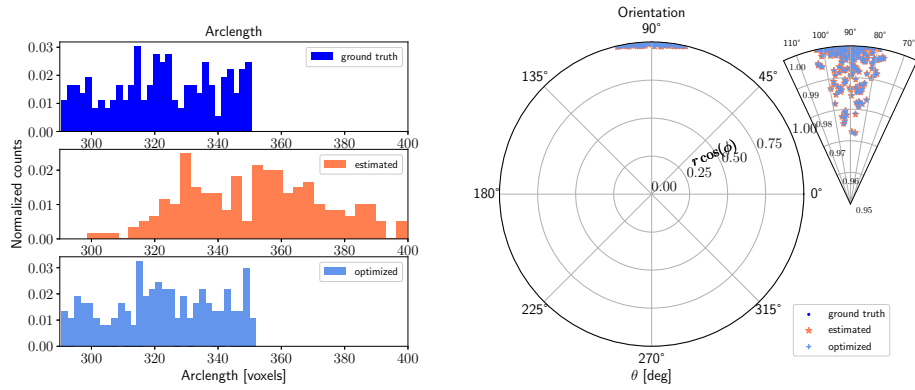
CRediT authorship contribution statement

Tim Elberfeld: Methodology, Software, Investigation, Writing - Original Draft, Writing - Review & Editing. **Jan Sijbers:** Conceptualization, Writing- Review & Editing, Supervision, Project Administration. **Jan De Beenhouwer:** Conceptualization, Writing- Review & Editing, Supervision, Project Administration.
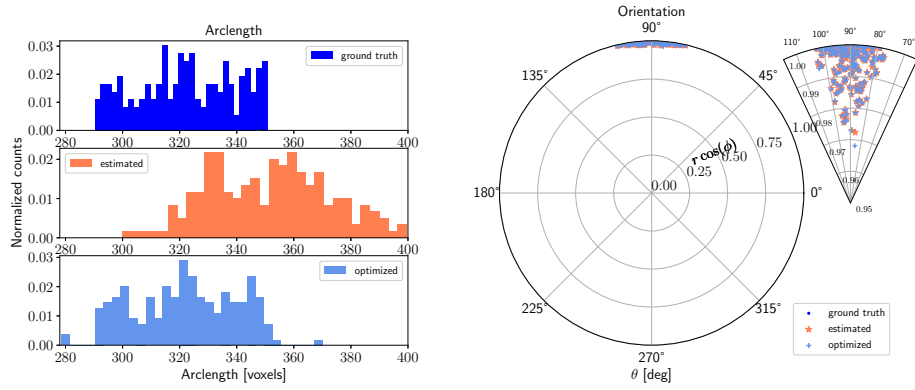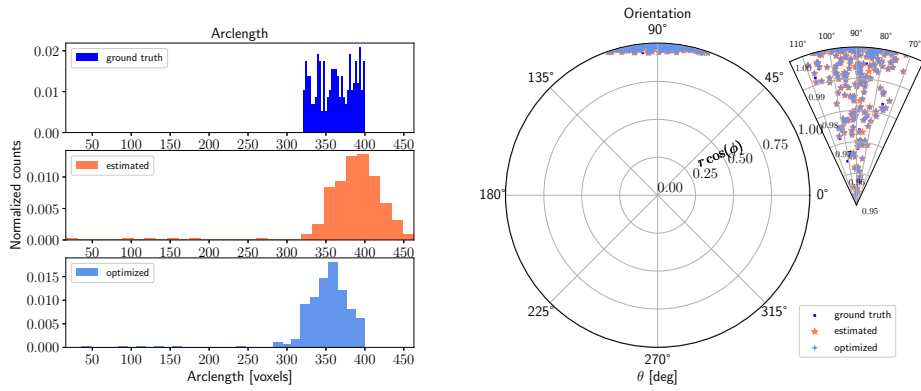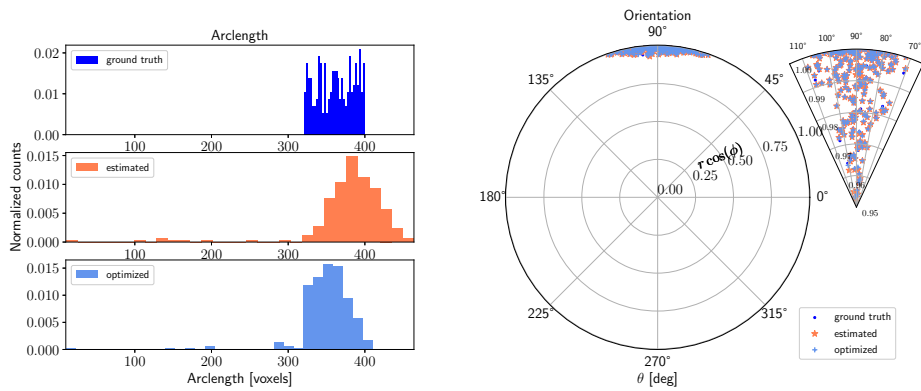
(a) *SimA*: **PARE**

(b) *SimA*: **cuPARE**

(c) *SimB*: **PARE**

(d) *SimB*: **cuPARE**

Figure 11: Length and orientation distributions for the simulated datasets in the ground truth, after detection (labeled *estimated*) and after optimization. To the right of the polar plot of the orientation a zoomed in wedge is shown to accentuate the spread of the values better.

To do…

☐ 1 (p. 7): discussion in results, then conclusion as positive

☐ 2 (p. 7): reduce size of section 2.2, 2.3